Nature does not rely on long-lived electronic quantum coherence for photosynthetic energy transfer

Hong-Guang Duan[a,b,c], Valentyn I. Prokhorenko[a], Richard J. Cogdell[d], Khuram Ashraf[d], Amy L. Stevens[a,c,e,f], Michael Thorwart[b,c,1], and R. J. Dwayne Miller[a,c,e,f,1]

[a]Atomically Resolved Dynamics Department, Max Planck Institute for the Structure and Dynamics of Matter, 22761 Hamburg, Germany; [b]I. Institut für Theoretische Physik, Universität Hamburg, 20355 Hamburg, Germany; [c]The Hamburg Center for Ultrafast Imaging, 22761 Hamburg, Germany; [d]Institute of Molecular, Cell, and Systems Biology, College of Medical, Veterinary, and Life Science, University of Glasgow, Glasgow G12 8QQ, United Kingdom; [e]Department of Chemistry, University of Toronto, Toronto, ON, Canada M5S 3H6; and [f]Department of Physics, University of Toronto, Toronto, ON, Canada M5S 3H6

Edited by Shaul Mukamel, University of California, Irvine, CA, and approved June 1, 2017 (received for review February 9, 2017)

During the first steps of photosynthesis, the energy of impinging solar photons is transformed into electronic excitation energy of the light-harvesting biomolecular complexes. The subsequent energy transfer to the reaction center is commonly rationalized in terms of excitons moving on a grid of biomolecular chromophores on typical timescales <100 fs. Today's understanding of the energy transfer includes the fact that the excitons are delocalized over a few neighboring sites, but the role of quantum coherence is considered as irrelevant for the transfer dynamics because it typically decays within a few tens of femtoseconds. This orthodox picture of incoherent energy transfer between clusters of a few pigments sharing delocalized excitons has been challenged by ultrafast optical spectroscopy experiments with the Fenna–Matthews–Olson protein, in which interference oscillatory signals up to 1.5 ps were reported and interpreted as direct evidence of exceptionally long-lived electronic quantum coherence. Here, we show that the optical 2D photon echo spectra of this complex at ambient temperature in aqueous solution do not provide evidence of any long-lived electronic quantum coherence, but confirm the orthodox view of rapidly decaying electronic quantum coherence on a timescale of 60 fs. Our results can be considered as generic and give no hint that electronic quantum coherence plays any biofunctional role in real photoactive biomolecular complexes. Because in this structurally well-defined protein the distances between bacteriochlorophylls are comparable to those of other light-harvesting complexes, we anticipate that this finding is general and directly applies to even larger photoactive biomolecular complexes.

2D spectroscopy | exciton | photosynthesis | Fenna–Matthews–Olson protein | quantum coherence

The principle laws of physics undoubtedly also govern the principle mechanisms of biology. The animate world consists of macroscopic and dynamically slow structures with a huge number of degrees of freedom, such that the laws of statistical mechanics apply. Conversely, the fundamental theory of the microscopic building blocks is quantum mechanics. The physics and chemistry of large molecular complexes may be considered as a bridge between the molecular world and the formation of living matter. A fascinating question since the early days of quantum theory is on the borderline between the atomistic quantum world and the classical world of biology. Clearly, the conditions under which matter displays quantum features or biological functionality are contrarious. Quantum coherent features only become apparent when systems with a few degrees of freedom with a preserved quantum mechanical phase relation of a wave function are well shielded from environmental fluctuations that otherwise lead to rapid dephasing. This dephasing mechanism is very efficient at ambient temperatures, at which biological systems operate. Also, the function of biological macromolecular systems relies on their embedding in a "wet" and highly polar solvent environment, which is again hostile to any quantum coherence. Therefore, the common view of multichromophoric Förster resonance energy transfer has been developed in which excitons are quantum-mechanically delocalized over a few neighboring pigments (1, 2), but a quantum coherent phase relation between the clusters involved in any biologically relevant dynamical process is rapidly destroyed on a sub-100-fs timescale. The transport is dominated by dipolar coupling between the sites with different energies, such that it is spatially directed and naturally leads to energy relaxation and flow to the reaction center. The nature of any quantum coherence is short-lived and could, at most, only involve a few neighboring sites—a view that is distinctively different from that of a largely quantum coherent process as implied by very long-lived electronic coherence living as long as proposed (3–5).

In recent years, ultrafast nonlinear 2D optical spectroscopy (6–8) has made it possible to challenge the orthodox view of the energy transfer because it can provide direct access to the couplings between excitonic states. A prominent energy transfer complex, which is simple enough to provide clean experimental spectroscopic data, is the Fenna–Matthews–Olson (FMO) protein (9). In 2007, the oscillatory beatings observed in the

Significance

We have revisited the 2D spectroscopy of the excitation energy transfer in the Fenna–Matthews–Olson (FMO) protein. Based on 2D spectroscopic signatures, the energy transfer dynamics in the FMO protein has been argued to be supported by long-lived electronic quantum coherence on timescales up to 1.5 ps. In contrast, our analysis, based on experimental data and confirmed by theoretical calculations, shows that the electronic decoherence occurs within 60 fs, in agreement with typical dephasing times in systems under these conditions. Given the relatively well-defined structure of the FMO protein, and comparative couplings between chlorophylls to other photosynthetic systems, the observed extremely fast decoherence should be viewed as general, bringing to question any significant quantum coherent transport contributions to photosynthesis.

Author contributions: V.I.P., M.T., and R.J.D.M. designed research; H.-G.D., V.I.P., A.L.S., and M.T. performed research; R.J.C. and K.A. contributed new reagents/analytic tools; H.-G.D., V.I.P., A.L.S., M.T., and R.J.D.M. analyzed data; and H.-G.D., V.I.P., R.J.C., M.T., and R.J.D.M. wrote the paper.

Conflict of interest statement: H.-G.D., V.I.P., and M.T. have a common publication in the *New Journal of Physics* with Shaul Mukamel as coauthor in 2015 on two-dimensional spectroscopy of a simple dye molecule. M.T. has a common publication with Shaul Mukamel in *The Journal of Chemical Physics* in 2014 on excitation energy transfer in molecules with orthogonal dipoles.

This article is a PNAS Direct Submission.

Freely available online through the PNAS open access option.

[1]To whom correspondence may be addressed. Email: michael.thorwart@physik.uni-hamburg.de or dwayne.miller@mpsd.mpg.de.

This article contains supporting information online at www.pnas.org/lookup/suppl/doi:10.1073/pnas.1702261114/-/DCSupplemental.

off-diagonal signals of 2D optical spectra have been reported to survive for >660 fs at cryogenic temperatures at 77 K (3). They were interpreted as signatures of long-lived electronic quantum coherent exciton dynamics in the FMO network. The same conclusion was also drawn from an experiment at higher temperatures up to 4° C (4), and similar beatings have been reported for marine cryptophyte algae (5) as well. These experiments have triggered an enormous interest in a potential new field of "quantum biology" (10–14), with far-reaching consequences, even for the functionality of the human brain (15) and for technological applications (16). The cornerstone experiments (3–5) remained unconfirmed until recently, when a new effort was made to identify the excitonic energy transfer pathways (17) at 77 K. However, observation of long-lived electronic coherences in the 2D off-diagonal signals was not mentioned in ref. 17.

Interesting conceptual studies on the possible constructive role of dephasing fluctuations on the efficiency of energy transfer in networks (18–23) were initiated subsequently. However, critical questions were also formulated (24–28), which remained largely unresolved up to present. Advanced dynamical simulations (29, 30) did not confirm long-lived electronic coherence and, as a consequence, wave-like energy transfer. An additional strong coupling of the excitonic to the nuclear degrees of freedom was also considered (31–39) as a possible driving source of coherence. Such a mechanism can yield longer-lived oscillations of the cross-peak amplitude (40, 41), yet, a strong vibronic coupling is required, and the oscillation amplitudes typically remain small. Moreover, in general, electronic coherence could only be enhanced by vibrational coherence if it lives at least as long as a single vibrational period lasts, an issue that has not been discussed.

Results

Motivated by the unsatisfactory lack of experimental confirmation of the long-lived electronic coherence at ambient temperatures, we have revisited this question in the present combined experimental and theoretical study, with the important distinction that we have conducted these studies under physiologically relevant conditions. We have measured a series of photon echo 2D optical spectra of the FMO trimer, extracted from green sulfur bacteria *Chlorobium tepidum*, at room temperature (296 K or 23° C) and for different waiting times T. The 2D spectra for selected times between $T=0$ and $T=2{,}000$ fs are shown in Fig. 1*A*. In addition, we have calculated the 2D spectra of the FMO monomer (see *SI Appendix* for details) and compared them to the experimental ones (Fig. 1*A*). In passing, we note that the calculated absorption spectrum shown in Fig. 1*C* coincides with that measured in ref. 42. The experimental and calculated 2D spectra for different waiting times agree well. At initial waiting time $T=0$, the 2D spectrum is stretched along the diagonal, which is a manifestation of a significant inhomogeneous broadening. With increasing waiting time, the inhomogeneous broadening is rapidly reduced and becomes undetectable beyond $T\sim 1{,}000$ fs. A central feature of 2D electronic spectroscopy is that the antidiagonal width uniquely reveals the electronic dephasing timescale. This property also holds when strong vibronic coupling is present (40). In Fig. 1*B*, we show the antidiagonal cut of the 2D spectrum measured at $T=0$

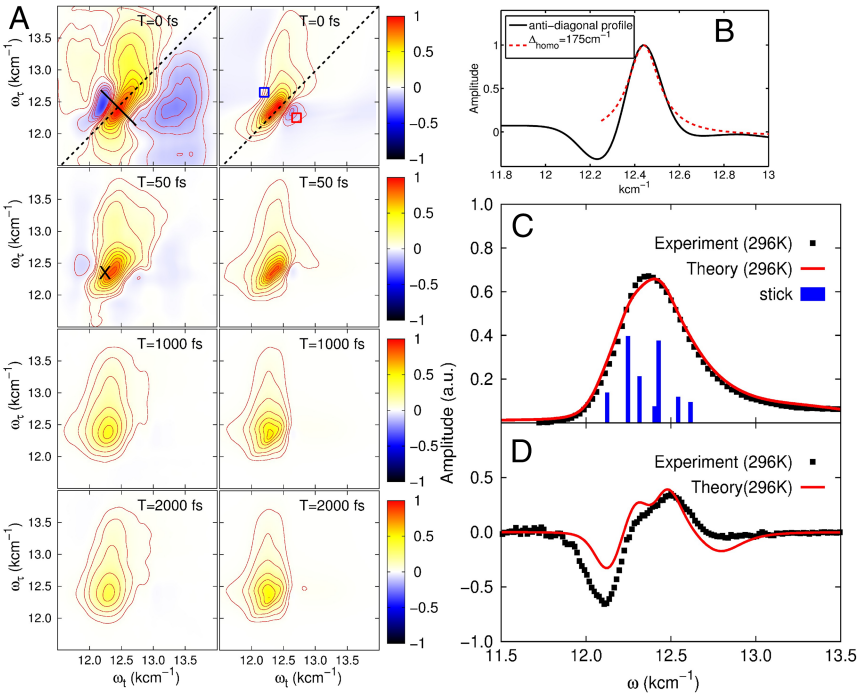

Fig. 1. (*A*) The 2D photon echo spectra for different waiting times *T* taken at 296 K. Shown is the real part. *A*, *Left* shows the experimental results, while *A*, *Right* displays the theoretically calculated spectra using the parameters obtained from the fits shown in *C* and *D*. The black solid line marks the antidiagonal along which the spectral signal is shown in *B*. It is used as a consistence check for the electronic dephasing time. The blue and red squares in the top right spectrum marks the spectral positions at which we evaluate the cross-peak time evolution shown in Fig. 3 *A* and *B*. In *A*, *Left*, the black cross in the second spectrum from the top marks the spectral position evaluated in Fig. 3*C*. (*B*) Spectral profile along the antidiagonal as extracted from the experimental data shown in *A*. We note that the negative amplitude part in the profile shows a mixed signal from the solvent and the excited state absorption at $T=0$ fs, which leads to a slight underestimation of the homogeneous line width. (*C*) Linear absorption spectrum at 296 K. Black symbols indicate the measured data, and the red solid line marks the theoretically calculated result. The blue bars show the calculated stick spectrum. (*D*) Circular dichroism (CD) spectrum at 296 K. Black symbols mark the measured data. The red solid lines show the theoretical result calculated with the same parameters as in *C*. a.u., arbitrary units.

(indicated in Fig. 1*A* by the black line) with a fitted Lorentzian profile yielding a FWHM of $\Delta_{\mathrm{hom}} = 175\ \mathrm{cm}^{-1}$, which corresponds to an electronic dephasing time of $\tau_{\mathrm{hom}} = [\pi c \Delta_{\mathrm{hom}}]^{-1} = 60$ fs (c is the speed of light). We note that the negative peaks in Fig. 1 *A* and *B* are due to a mixed photon echo signal with contributions from the solvent and the excited state absorption (6–8). The mixed photon echo signal gives 50 counts (cts) for the solvated FMO, and, in the absence of FMO, we have detected 10 cts. The solvent signal completely disappears for waiting times up to 20–30 fs. Therefore, we estimate that the solvent (FMO excited state absorption) contribution to the negative peak is $\sim 20\%$ (80%). Furthermore, the magnitude of the off-diagonal peaks in the upper left region of the 2D spectra remarkably increases for growing waiting times. The spectrum becomes strongly elongated along the ω_τ coordinate and reveals an efficient energy transfer between the FMO pigments (6–8). The progressions ranging from the central peak at $\omega_\tau = \omega_t = 12{,}400\ \mathrm{cm}^{-1}$ to the region $\omega_\tau = 13{,}500\ \mathrm{cm}^{-1}$, $\omega_t = 12{,}400\ \mathrm{cm}^{-1}$ indicate a vibrational relaxation of the localized vibrational modes of the bacteriochlorophylls. In addition, we clearly observe a fast decay of the central peak amplitude within the first $1-2$ ps, induced by thermally fluctuating electric fields from the polar protein environment.

The energy transfer pathways and the associated timescales are revealed by a multidimensional global analysis (43) of consecutive 2D spectra at different waiting times T, arranged in a 3D array $S(\omega_\tau, \omega_t, T)$ (for a detailed description, see supporting information in ref. 44). This results in 2D decay-associated spectra (2DDAS) $A_i(\omega_\tau, \omega_t)$, which are shown in Fig. 2*A* (*Left*, analyzed experimental spectra; *Right*, analyzed theoretical data; see also *SI Appendix* for more details). We have resolved four different energy transfer timescales. The shortest decay time, $\tau_1 = 90$ fs, is mainly associated to the electronic dephasing of the diagonal peak at $12{,}500\ \mathrm{cm}^{-1}$. Furthermore, a strong negative off-diagonal peak at ($\omega_\tau = 12{,}500\ \mathrm{cm}^{-1}$, $\omega_t = 12{,}000\ \mathrm{cm}^{-1}$) indicates a rapid loss of absorption in the 2D spectra. This feature illustrates contributions from the energy transfer process from the excitonic states located around $12{,}500\ \mathrm{cm}^{-1}$ to the lower ones at $12{,}000\ \mathrm{cm}^{-1}$. The second 2DDAS, associated with a lifetime of $\tau_2 = 750$ fs, displays a similar feature, but with slightly broader peaks and a noticeable extension to the blue spectral side. The third ($\tau_3 = 7.0$ ps) and fourth ($\tau_4 = \infty$) components of the 2DDAS only show one diagonal peak at the central position of $12{,}200\ \mathrm{cm}^{-1}$ with rather broad peaks. This observation indicates a thermal relaxation of the pigments inside the FMO protein. Our findings qualitatively agree with those in ref. 17, with all our dephasing times being shorter, which is due the difference in temperature between 77 K and the present studies under ambient conditions.

Next, we address the question of long-lived coherent oscillations in off-diagonal signals in the 2D spectra. We have analyzed the residuals obtained after removing the underlying slow kinetics from the 3D dataset $S(\omega_\tau, \omega_t, T)$. Their Fourier transform provides a 3D spectrum of the possible vibrations. The most intense of them, with the amplitudes above the noise threshold, are plotted in *SI Appendix*, Figs. S9 and S10. As a result of our model, all of the exciton states in the FMO complex are located in the frequency region of $12{,}123$–$12{,}615\ \mathrm{cm}^{-1}$. Hence, the largest oscillation frequency that can be expected from the beatings between them is $\sim 490\ \mathrm{cm}^{-1}$. However, the lowest oscillation frequency that we found in the residuals lies well above ($\sim 600\ \mathrm{cm}^{-1}$). Hence, we can safely conclude that the origin of these oscillations is not due to interference between the excitonic states.

A cross-correlation analysis (44) of the residuals across the diagonal $\omega_\tau = \omega_t$ in a delay time window up to 2 ps yields a 2D correlation spectrum shown in Fig. 2*B*, where the (negative) positive values indicate (anti)correlated residuals. We find two strong negative peaks, which proves on the basis of refs. 45 and 46 that the oscillations in this region are related to vibrational coherence. Moreover, we clearly observe two negative peaks at the frequencies $12{,}400\ \mathrm{cm}^{-1}$ and $13{,}300\ \mathrm{cm}^{-1}$. They can be associated to strong localized vibrational modes of the bacteriochlorophylls, which follows from the vibrational progression in the absorption spectrum (*SI Appendix*, Fig. S2*A*).

To underpin the vibrational origin of the oscillations with rather small amplitudes, we consider the time evolution of the

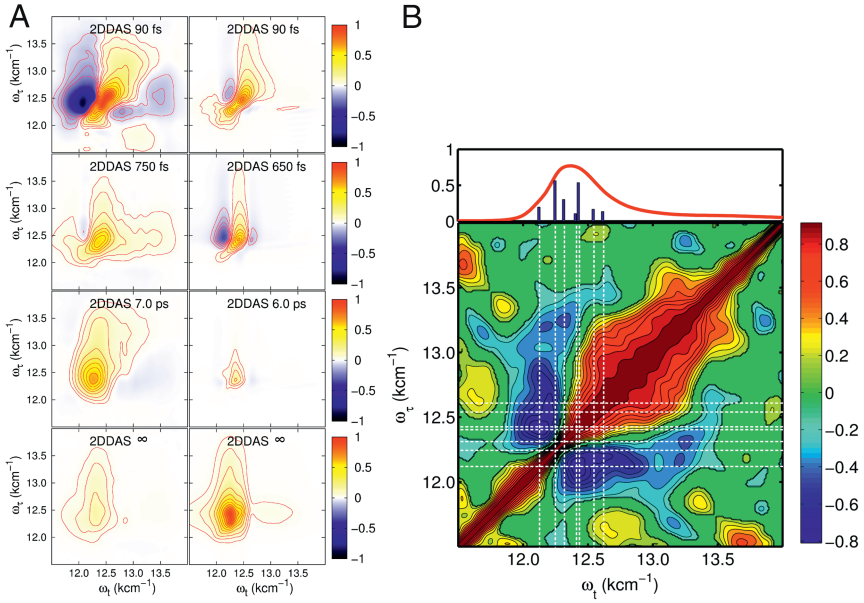

Fig. 2. (*A*) The 2DDAS. *A*, *Left* shows the experimental results, and *A*, *Right* shows the theoretically calculated spectra. The four resulting associated decay times $\tau_{1,\ldots,4}$ are indicated in the spectra. (*B*) The 2D correlation map of residuals obtained from the series of experimental spectra after subtracting the kinetics by the global fitting procedure. The red line on top is the measured absorption spectrum of the FMO trimer, and the blue bars mark the stick spectrum of the FMO model. The white dashed lines mark the exciton energies, which are used to overlap with the correlation map.

two off-diagonal signals located at the pair of frequencies 12,300 cm^{-1} and 12,600 cm^{-1}, marked by the red and blue squares in Fig. 1*A*. We consider the results of the theoretical modeling, which explicitly only includes an overdamped vibrational mode (with a vibrational lifetime of $\tau_\Gamma = 15$ fs; *SI Appendix*), but does not include underdamped vibrational states of the bacteriochlorophylls. Hence, any calculated oscillations occurring out to long time must originate from possible beatings of the electronic dynamics due to a coherent coupling between the excitonic states. This feature helps to uniquely determine the origin of the oscillations observed in the experimental spectra. The results shown in Fig. 3 *A* and *B* illustrate that any electronic coherence between excitonic states vanishes within a dephasing time window of ~ 60 fs. It is interesting to point out that this value of the dephasing time agrees with the time of the dephasing measured by the antidiagonal bandwidth of the 2D spectrum at $T = 0$ fs. In fact, when the fluctuations are fast, the timescales of homogeneous and inhomogeneous broadening are well separated, and we are in the fast modulation or homogeneous limit. The resulting exciton dynamics is then Markovian, and, in this limit, the antidiagonal (or homogeneous) line width and the electronic dephasing time coincide (47, 48). The Markovian character of the exciton dynamics is revealed by the exponentially decaying frequency correlation function (48), which can be extracted by measuring the ellipse eccentricity (49) of the 2D spectra as a function of the waiting time (*SI Appendix*, Fig. S13). In addition, in the numerically exact calculation of ref. 50, the non-Markovianity measure of the FMO exciton dynamics has been calculated to be zero. Furthermore, the excellent agreement between the experimental and theoretical values of the antidiagonal bandwidth demonstrates the validity of our model to capture the damping induced by the thermal noise. In addition, our direct observation of the homogeneous linewidth in this fast modulation limit is in agreement with the independent FMO data of ref. 17 (*SI Appendix*, Fig. S6). This study finds an ~ 100 cm^{-1} homogeneous line width estimated from the low-temperature data at 77 K. The resulting electronic dephasing time can be calculated from our model with all of the parameters kept unchanged except the temperature. We find 110 fs (*SI Appendix*, Fig. S7). In fact, if long-lived electronic coherence were operating on the 1-ps timescale as claimed perviously (3), the electronic dephasing should be significantly reduced due to a weaker exciton–phonon interaction. The corresponding antidiagonal line width of the 2D spectrum would have to be on the order of 10 cm^{-1} (*SI Appendix*, Fig. S8) and would appear as an extremely (unrealistically) sharp ridge in the inhomogeneously broadened 2D spectrum. The lack of this feature conspicuously points to the misassignment of the long-lived features to long-lived electronic coherences, which, as now established in the present work, is due to weak vibrational coherences. The frequencies of these oscillations, their lifetimes, and amplitudes all match those expected for molecular modes (51, 52), and not long-lived electronic coherences.

For a comparison with the previous experimental work [at the temperature 277 K (4° C) of ref. 4], we have extracted from our measured 2D spectra the time evolution of the "cross-peak" located at $\omega_\tau = 12{,}350$ cm^{-1}, $\omega_t = 12{,}200$ cm^{-1} (spectral position marked by a black cross in Fig. 1*A*). As follows from Fig. 3*C* (see also *SI Appendix*), no long-lived beatings and associated electronic coherence can be observed at this position in the measured 2D spectra. Within the available experimental signal-to-noise ratio, we can conclude that there are no oscillations with amplitudes $>5\%$ of the signal. They may be interpreted as weak vibrational coherence, consistent with earlier findings (41) for a much smaller excitonically coupled system (a dimer) with strong vibronic coupling.

Conclusion

The present work provides a full analysis of possible electronic state couplings, decay-associated spectra, signs/amplitudes of off-diagonal features, and, most telling, the directly determined homogeneous lineshape, and thus shows that the previous assignment of weak long-lived oscillatory signals in 2D spectra to long-lived electronic coherences is incorrect. There is no long-range coherent energy transport occurring in the FMO complex and, in all cases, is not needed to explain the overall efficiency of energy transfer. This finding constitutes the main result of our work and confirms the orthodox picture of rapidly decaying electronic coherence on a timescale of 60 fs in the exciton dynamics in the FMO protein complex at ambient temperature. In turn, contributions of quantum coherence to biological functionality under ambient conditions in natural light-harvesting units is extremely unlikely, a finding being in line with our previous study of the light-harvesting complex LHCII (44). Because the FMO complex is rather small and a structurally quite well-defined protein, with the distances between bacteriochlorophylls comparable to other natural light-harvesting systems, we anticipate that this finding is generic and also applies to even larger photoactive biomolecular complexes.

Materials and Methods

Experimental Setup. Ultrashort coherent light pulses were generated by a home-built noncollinear optical parametric amplifier pumped by a commercial femtosecond laser Pharos (Light Conversion). A broadband spectrum with a FWHM of 100 nm was centered at the wavelength of 770 nm

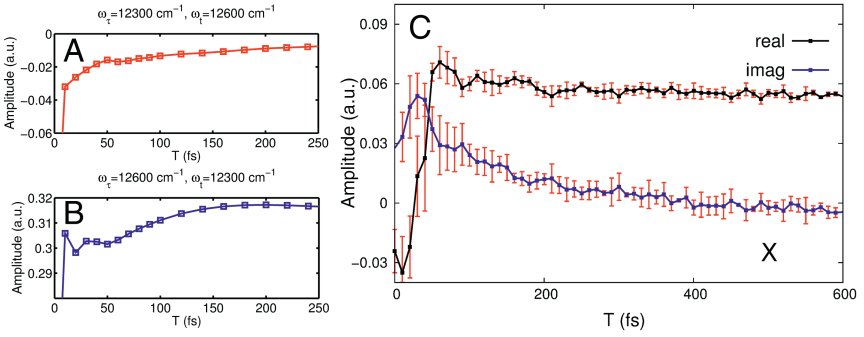

Fig. 3. (*A* and *B*) Time evolution of the real part of the calculated 2D photon echo signal at the spectral positions $\omega_\tau = 12{,}300$ cm^{-1}, $\omega_t = 12{,}600$ cm^{-1} marked by a red square in Fig. 1*A* (*A*) and for $\omega_\tau = 12{,}600$ cm^{-1}, $\omega_t = 12{,}300$ cm^{-1} marked by a blue square in Fig. 1*A* (*B*). It is apparent that a minimal amount of electronic coherence only survives up to ~ 60 fs. (*C*) The real (black) and imaginary (blue) part of the experimentally measured time trace at the same spectral position (black cross in Fig. 1*A*) $\omega_\tau = 12{,}350$ cm^{-1}, $\omega_t = 12{,}200$ cm^{-1} as measured in ref. 4, however, measured here at 296 K. The error bars indicate the SD obtained after averaging four datasets. The imaginary part is vertically shifted by 0.035 for clarity. a.u., arbitrary units.

and overlapped the Q_y absorption band of the FMO antenna complex (*SI Appendix*, Fig. S2*A*). The laser pulses were compressed to the transform-limited with the pulse duration of 16 fs FWHM by a combination of a prism compressor (F2) and a deformable mirror shaper (OKO Technologies). Their temporal profiles were characterized by means of the frequency-resolved optical gating (FROG) measured in situ by using a 1-mm fused silica window. The measured FROG traces were analyzed by using a commercial program, FROG3 (Femtosecond Technologies). The 2D spectra were collected in an all-reflective 2D spectrometer based on a diffractive optic (Holoeye) with a phase stability of $\lambda/160$, whose configuration is described elsewhere (53), equipped with the Sciencetech spectrometer model 9055 and a high-sensitive CCD linear array camera (Entwicklungsbüro Stresing). To avoid possible annihilation of excitons in the FMO trimer, the excitation energy was kept at $<$12 nJ per beam. Under this excitation condition, the magnitude of the homodyne photon-echo signal was proportional to the third power of the incoming pulse energy, which confirms the regime of linear excitation (*SI Appendix*, Fig. S2*B*). The 2D spectra were collected at each fixed waiting time T by scanning the delay $\tau = t_1 - t_2$ in the range of $[-128$ fs, 128 fs] with a delay step of 1 fs. At each delay point, 150 spectra were averaged. The waiting time $T = t_3 - t_2$ was linearly scanned within the range of $0 - 2$ ps in steps of 10 fs and with logarithmically spaced delay time steps up to 10 ps.

Sample Preparation and Measuring Condition. The FMO protein was isolated from the green sulfur bacteria *C. tepidum* (see *SI Appendix* for details). Before each series of measurements, the sample was filtered with a 0.2 μm filter to reduce light scattering. The absorption spectrum was recorded by using a Shimadzu spectrometer (UV-2600) in a cell of 1-mm optical path length. To avoid the influence of the sample degradation (see *SI Appendix* for details), the cell in the 2D setup was placed on a precise 2D translator and moved at a speed of $\sim$20 cm/s in both directions. The excitation spot diameter on the sample was $\sim$80 μm. In the experiments, we used a 1-mm quartz cell (Starna). We did not detect any noticeable difference of the measured spectra when a 0.5-mm cell was used.

Theoretical Model. We considered a standard molecular model of the FMO monomer described by the Hamiltonian H_{mol} and consisting of seven bacteriochlorophylls in the single-excitation subspace. Double excitation played no role at the considered weak spectroscopic field strengths. Recently, an eighth pigment in the FMO complex was found (54). However, its spatial distance from the other seven pigments is very large, and it is very likely that this pigment is removed in the majority of the complexes during the isolation procedure (17, 54). The model parameters (i.e., the site energies ϵ_m and the electronic couplings $J_{n,m}$) were taken from ref. 55. The spectral density of the bath is given in *SI Appendix*. During the procedure of fitting the model to the measured absorption and CD spectra, we kept the electronic coupling elements unchanged and optimized the site energies. To fit the absorption and CD spectra simultaneously, we optimized the site energies and the inhomogeneous broadening, which accounts for the static disorder. In particular, we chose a Gaussian distribution with a FWHM of 90 cm^{-1}, except for site 3, for which we found that it was necessary to reduce the static disorder to 54 cm^{-1} of FWHM to fit the absorption peak of 12,150 cm^{-1} at 77 K (the low-temperature calculations in comparison with the experimental spectra are shown in *SI Appendix*). To obtain converged results, 500 calculated spectra were included in the average. The orientations of the transition dipole moments were taken from Protein Data Bank ID code 3ENI (56), and the magnitudes of the transition dipole moments were assumed to all be 4 Debye. The modeling has been additionally verified (*SI Appendix*) by comparing the calculated results for the time-dependent FMO site populations with available exact numerical calculations (29).

ACKNOWLEDGMENTS. H.-G.D. thanks Eike-Christian Schulz for his comments on the properties of the FMO protein at room temperature. This work was supported by the Max Planck Society and the Hamburg Center for Ultrafast Imaging within the German Excellence Initiative supported by the Deutsche Forschungsgemeinschaft. H.-G.D. was supported generously by the Joachim-Hertz-Stiftung Hamburg. Work at the University of Glasgow was supported as part of the Photosynthetic Antenna Research Center, an Energy Frontier Research Center funded by the US Department of Energy, Office of Science, Basic Energy Sciences Award DE-SC0001035.

1. Förster T (1948) Zwischenmolekulare energiewanderung und fluoreszenz. *Ann Phys* 437:55–75.
2. Jang S, Newton M, Silbey RJ (2004) Multichromophoric Forster resonance energy transfer. *Phys Rev Lett* 92:218301.
3. Engel GS, et al. (2007) Evidence for wavelike energy transfer through quantum coherence in photosynthetic systems. *Nature* 446:782–786.
4. Panitchayangkoon G, et al. (2010) Long-lived quantum coherence in photosynthetic complexes at physiological temperature. *Proc Natl Acad Sci USA* 107:12766–12770.
5. Collini E, et al. (2010) Coherently wired light-harvesting in photosynthetic marine algae at ambient temperature. *Nature* 463:644–647.
6. Mukamel S (2000) Multidimensional femtosecond correlation spectroscopies of electronic and vibrational excitations. *Annu Rev Phys Chem* 51:691–729.
7. Woutersen S, Hamm P (2002) Nonlinear two-dimensional vibrational spectroscopy of peptides. *J Phys Condens Mat* 14:R1035.
8. Jonas DM (2003) Two-dimensional femtosecond spectroscopy. *Annu Rev Phys Chem* 54:425–463.
9. Fenna RE, Matthews BW, Olson JM, Shaw EK (1974) Structure of a bacteriochlorophyll-protein from the green photosynthetic bacterium Chlorobium limicola: Crystallographic evidence for a trimer. *J Mol Biol* 84:231–240.
10. Ball P (2011) Physics of life: The dawn of quantum biology. *Nature* 474:272–274.
11. Scholes GD, Fleming GR, Olaya-Castro A, van Grondelle R (2011) Lessons from nature about solar light harvesting. *Nat Chem* 3:763–774.
12. Lambert N, et al. (2013) Quantum biology. *Nat Phys* 9:10–18.
13. Huelga SF, Plenio M (2013) Vibrations, quanta and biology. *Contemp Phys* 54:181–207.
14. Mohseni M, Omar Y, Engel GS, Plenio M (2014) *Quantum Effects in Biology* (Cambridge Univ Press, Cambridge, MA).
15. Abbott D, Davies P, Pati A (2010) *Quantum Aspects of Life* (World Scientific, Singapore).
16. Olaya-Castro A, Nazir A, Fleming GR (2012) Quantum-coherent energy transfer: Implications for biology and new energy technologies. *Philos Trans R Soc Lond A Math Phys Eng Sci* 370:3613–3617.
17. Thyrhaug E, Žídek K, Dostál J, Bina D, Zigmantas D (2016) Exciton structure and energy transfer in the Fenna-Matthews-Olson complex. *J Phys Chem Lett* 7:1653–1660.
18. Plenio M, Huelga SF (2008) Dephasing-assisted transport: Quantum networks and biomolecules. *New J Phys* 10:113019.
19. Mohseni M, Rebentrost P, Lloyd S, Aspuru-Guzik A (2008) Environment-assisted quantum walks in photosynthetic energy transfer. *J Chem Phys* 129:174106.
20. Olaya-Castro A, Lee CF, Fassioli Olsen F, Johnson NF (2008) Efficiency of energy transfer in a light-harvesting system under quantum coherence. *Phys Rev B* 78:085115.
21. Thorwart M, Eckel J, Reina JH, Nalbach P, Weiss S (2009) Enhanced quantum entanglement in the non-Markovian dynamics of biomolecular excitons. *Chem Phys Lett* 478:234–237.
22. Sarovar M, Ishizaki A, Fleming GR, Whaley KB (2010) Quantum entanglement in photosynthetic light-harvesting complexes. *Nat Phys* 6:462–467.
23. Walschaers M, Fernandez-de-Cossio Diaz J, Mulet R, Buchleitner A (2013) Optimally designed quantum transport across disordered networks. *Phys Rev Lett* 111:180601.
24. Wilde MM, McCracken JM, Mizel A (2010) Could light harvesting complexes exhibit non-classical effects at room temperature? *Proc Math Phys Eng Sci* 466:1347–1363.
25. Briggs JS, Eisfeld A (2011) Equivalence of quantum and classical coherence in electronic energy transfer. *Phys Rev E* 83:051911.
26. Miller WH (2012) Perspective: Quantum or classical coherence? *J Chem Phys* 136:210901.
27. Mukamel S (2013) Comment on "Coherence and uncertainty in nanostructured organic photovoltaics". *J Phys Chem A* 117:10563–10564.
28. Halpin A, Johnson PJM, Miller RJD (2014) Comment on "Engineering coherence among excited states in synthetic heterodimer systems". *Science* 344:1099.
29. Nalbach P, Braun D, Thorwart M (2011) Exciton transfer dynamics and quantumness of energy transfer in the Fenna-Matthews-Olson complex. *Phys Rev E* 84:041926.
30. Olbrich C, Strümpfer J, Schulten K, Kleinekathöfer U (2011) Theory and simulation of the environmental effects on FMO electronic transitions. *J Phys Chem Lett* 2:1771–1776.
31. Christensson N, Kauffmann HF, Pullerits T, Mančal T (2012) Origin of long-lived coherences in light-harvesting complexes. *J Phys Chem B* 116:7449–7454.
32. Kreisbeck C, Kramer T (2012) Long-lived electronic coherence in dissipative exciton dynamics of light-harvesting complexes. *J Phys Chem Lett* 3:2828–2833.
33. Hossein-Nejad H, Olaya-Castro A, Scholes GD (2012) Phonon-mediated path-interference in electronic energy transfer. *J Chem Phys* 136:024112.
34. Kolli A, O'Reilly EJ, Scholes GD, Olaya-Castro A (2012) The fundamental role of quantized vibrations in coherent light harvesting by cryptophyte algae. *J Chem Phys* 137:174109.
35. Nalbach P, Thorwart M (2012) The role of discrete molecular modes in the coherent exciton dynamics in FMO. *J Phys B At Mol Opt Phys* 45:154009.
36. Chin AW, et al. (2013) The role of non-equilibrium vibrational structures in electronic coherence and recoherence in pigment-protein complexes. *Nat Phys* 9:113–118.
37. O'Reilly EJ, Olaya-Castro A (2014) Non-classicality of molecular vibrations activating electronic dynamics at room temperature. *Nat Comm* 5:3012.
38. Mujica-Martinez C, Nalbach P (2015) On the influence of underdamped vibrations on coherence and energy transfer times in light-harvesting complexes. *Ann Phys* 527:592–600.
39. Butkus V, Valkunas L, Abramavicius D (2014) Vibronic phenomena and exciton-vibrational interference in two-dimensional spectra of molecular aggregates. *J Chem Phys* 140:034306.
40. Halpin A, et al. (2014) Two-dimensional spectroscopy of a molecular dimer unveils the effects of vibronic coupling on exciton coherences. *Nat Chem* 6:196–201.

41. Duan HG, Nalbach P, Prokhorenko VI, Mukamel S, Thorwart M (2015) On the nature of oscillations in two-dimensional spectra of excitonically-coupled molecular systems. *New J Phys* 17:072002.
42. Wen J, Zhang H, Gross ML, Blankenship RE (2009) Membrane orientation of the FMO antenna protein from *Chlorobaculum tepidum* as determined by mass spectrometry-based footprinting. *Proc Natl Acad Sci USA* 106:6134–6139.
43. Prokhorenko VI (2012) Global analysis of multi-dimensional experimental data. *Eur Photochem Assoc Newsl*:21–23.
44. Duan HG, et al. (2015) Two-dimensional electronic spectroscopy of light harvesting complex II at ambient temperature: A joint experimental and theoretical study. *J Phys Chem B* 119:12017–12027.
45. Butkus V, Zigmantas D, Valkunas L, Abramavicius D (2012) Vibrational vs. electronic coherence in 2D spectrum of molecular systems. *Chem Phys Lett* 545:40–43.
46. Egorova D (2008) Detection of electronic and vibrational coherences in molecular systems by 2D electronic photon echo spectroscopy. *Chem Phys* 347:166–176.
47. Mukamel S (1995) Continuous distribution of oscillators: Dephasing and relaxation. *Principles of Nonlinear Optical Spectroscopy* (Oxford Univ Press, Oxford), pp 221–226.
48. Hamm P, Zanni M (2011) Homogeneous and inhomogeneous dynamics. *Concepts Methods 2D Infrared Spectroscopy* (Cambridge Univ Press, Cambridge, UK), pp 152–164.
49. Lazonder K, Pshenichnikov MS, Wiersma DA (2007) Two-dimensional optical correlation spectroscopy applied to liquid/glass dynamics. *Ultrafast Phenomena XV, Proceedings of the 15th International Conference*, eds Corkum P, Jonas DM, Miller RJD, Weiner AM (Springer, Berlin), pp 356–358.
50. Mujica-Martinez C, Nalbach P, Thorwart M (2013) Quantification of non-Markovian effects in the Fenna-Matthews-Olson complex. *Phys Rev E* 88:062719.
51. Rätsep M, Freiberg A (2007) Electron-phonon and vibronic coupling in the FMO bacteriochlorophyll a antenna complex studied by difference fluorescence line narrowing. *J Lumin* 127:251–259.
52. Rätsep M, Cai Z-L, Reimers JR, Freiberg A (2011) Demonstration and interpretation of significant asymmetry in the low-resolution and high-resolution Qy fluorescence and absorption spectra of bacteriochlorophyll a. *J Chem Phys* 134:024506.
53. Prokhorenko VI, Picchiotti A, Maneshi S, Miller RJD (2015) Broadband electronic two-dimensional spectroscopy in the deep UV. *Ultrafast Phenomena XIX. Springer Proceedings in Physics*, eds Yamanouchi K, Cundiff S, de Vivie-Riedle R, Kuwata-Gonokami M, DiMauro L (Springer, Cham, Switzerland), Vol 16, pp 432–435.
54. Schmidt am Busch M, Müh F, El-Amine Madjet M, Renger T (2011) The eighth bacteriochlorophyll completes the excitation energy funnel in the FMO protein. *J Phys Chem Lett* 2:93–98.
55. Adolphs J, Renger T (2006) How proteins trigger excitation energy transfer in the FMO complex of green sulfur bacteria. *Biophys J* 91:2778–2797.
56. Tronrud DE, Wen J, Gay L, Blankenship RE (2009) The structural basis for the difference in absorbance spectra for the FMO antenna protein from various green sulfur bacteria. *Photosynth Res* 100:79–87.

Supporting Information Appendix to

Nature does not rely on long-lived electronic quantum coherence for photosynthetic energy transfer

Hong-Guang Duan, Valentyn I. Prokhorenko, Richard J. Cogdell, Khuram Ashraf, Amy L. Stevens, Michael Thorwart*, R. J. Dwayne Miller*

*Corresponding authors.

E-mail: michael.thorwart@physik.uni-hamburg.de, dwayne.miller@mpsd.mpg.de

Preparation of the FMO protein

The Fenna-Matthews-Olson (FMO) protein complex was prepared from cells of the thermophilic green sulfur bacterium *Chlorobium tepidum*. A strain of *C. tepidum* that had been engineered to produce a His-tagged version of its reaction center was used in order to simplify the purification strategy. This strain was a gift of Prof. Oh-Oka (*1*). The cells were grown anaerobically in the light in modified Pfennig's media (*2*). New cultures were allowed to go fully anaerobic in the dark overnight, then they were grown at a light intensity of about 30 micromoles photons $m^{-2}s^{-1}$ at 43° C for 2 to 3 days. When fully grown, the cells were harvested by centrifugation at 12,000 x g for 20 min. The reaction centres (which bind FMO) were isolated from broken cells (*3*). At the stage of the nickel affinity column chromatography a high salt wash at 500 mM NaCl elutes the FMO complexes. This dilute solution of FMO was then purified by a combination of ion exchange chromatography on a Whatrman DE52 cellulose resin and size exclusion chromatography on a Sepharose S-200 column.

Sample condition at room temperature

Before doing the measurement, we have checked the thermal degradation of the sample for different temperatures. The sample was kept under -80° C in the freezer. Before measuring the circular dichroism (CD) spectrum, we have warmed up the sample by putting it on the table for about half an hour. Then, we have recorded the CD spectrum in the UV region at the temperature of 23° C, at which we have recorded the 2D spectra. The result of the CD spectrum is shown in Fig. S1 (a). We extract the structure information of the FMO protein by measuring

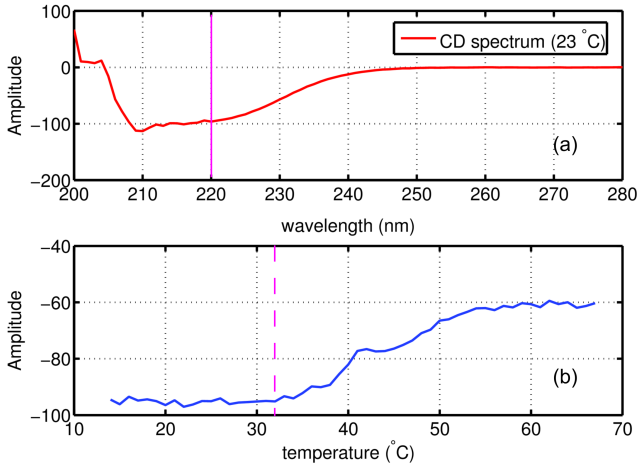

Figure S1: (a) Circular dichroism (CD) spectrum of the FMO complex in the UV regime at room temperature (23° C). The magenta solid line marks the wave length of 220 nm at which we detect the sample condition. (b) CD spectral signal at 220 nm for varying temperature. The magenta dashed line marks the temperature (32° C) above which thermal degradation of the FMO protein sets in.

the signal changes at the wave length of 220 nm (*4, 5*). Usually, the signal at this frequency is considered as originating from the protein. It shows a relatively strong magnitude with a weak noisy background. It is marked by the magenta line in the Fig. S1 (a). Then, we have recorded the CD spectra at different temperatures starting from 14 to 67° C. The result of the CD spectral signal at 220 nm for different temperatures is shown in Fig. S1 (b). We observe that the CD signal is stable and shows $\sim$ 95 counts below 32° C. Above 32° C, the magnitude of the CD signal at 220 nm rapidly decays to 60 counts. This indicates that the structure of the protein experiences thermal damage. We have repeated the detection five times at each temperature and show the corresponding average in the figure.

Laser excitation spectrum and field strength

The excitation spectrum of the laser used was a broadband spectrum with a FWHM of 100 nm, centered at the wavelength of 770 nm and overlapped the Q_y absorption band of the FMO antenna complex (see Fig. S2 (a)). The excitation energy was kept below 12 nJ per beam to stay in the weak-field regime of linear excitation. The magnitude of the detected homodyne photon-echo signal was proportional to the third power of the incoming pulse energy, see Fig. S2 (b).

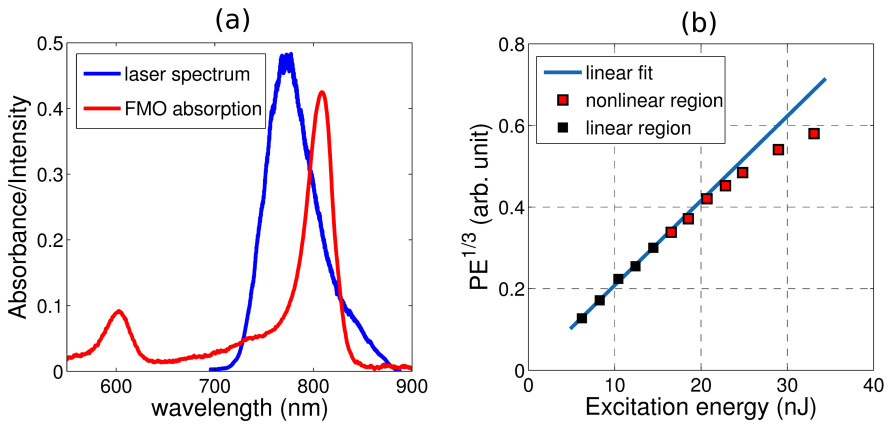

Figure S2: (a) Laser excitation spectrum (blue line) and absorption spectrum (red line) of the FMO complex at room temperature. (b) Dependence of the homodyne photon echo signal on the excitation energy measured at zero waiting time. To illustrate the deviation from the linear region, we plot the cubic root of the magnitude of the photon echo signal on the ordinate.

Spectral density

For simplicity, we choose an Ohmic spectral density to characterize the environmental fluctuations. In addition, to account for the weak vibrational progression detected in the absorption spectrum of the FMO complex (see Fig. 1C in the main paper), we have to add one additional vibrational mode in the spectral density. We find an optimal fit if we assume this component to be of the form of an overdamped harmonic mode to phenomenologically cover the experimentally observed vibrational sidebands in the linear spectrum (*6*). Therefore, the total spectral density used throughout the work is

$$J(\omega) = \gamma\omega e^{-\omega/\omega_c} + \frac{2}{\pi} S\Omega^3 \frac{\omega\Gamma}{(\Omega^2-\omega^2)^2+\omega^2\Gamma^2}\,. \tag{S1}$$

Here, γ is the Ohmic damping constant and ω_c is a high-frequency cut-off parameter. Moreover, S is the Huang-Rhys factor, Ω is the vibrational frequency of the overdamped mode and Γ is the lifetime broadening. From fitting the linear absorption spectrum, we find $\gamma = 0.7$, $\omega_c = 350$ cm^{-1}, $S = 0.12$, $\Omega = 900$ cm^{-1} and $\Gamma = 700$ cm^{-1}. The reorganization energy can be calculated as $\lambda = \frac{2}{\pi}\gamma\omega_c + \frac{1}{\pi}S\Omega = 190$ cm^{-1}. The spectral density is shown in Fig. S3.

Time non-local quantum master equation

For the numerical simulations, we have applied the established method of the time non-local quantum master equation (*7, 8*). Time evolution of the total density matrix ρ which includes system and bath is governed by the Liouville-von Neumann equation with the Liouville super-

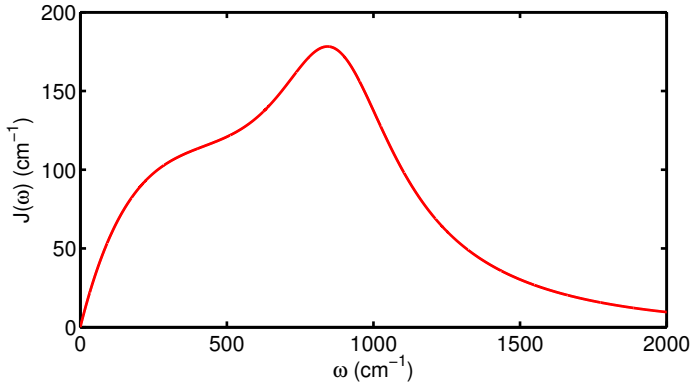

Figure S3: Spectral density used in this work for modeling the dissipative exciton dynamics. The overdamped mode yields the accurate vibrational progression in the absorption spectrum of the FMO complex shown in Fig. 1C in the main paper.

operator $\mathcal{L}$ ($\hbar = 1$), according to

$$\dot{\rho}_{\rm tot} = -i[H_{\rm tot}, \rho_{\rm tot}] = \mathcal{L}\rho_{\rm tot}\,. \tag{S2}$$

The total Hamiltonian $H_{\rm tot} = H_{\rm s} + H_{\rm b} + \lambda H_{\rm sb} + \lambda^2 H_{\rm ren}$ includes the system, the bath, and interaction and renormalization terms. For the sake of concreteness, let us assume here a system with a single degree of freedom x. The bath consists of an ensemble of harmonic oscillators with the Hamiltonian $H_{\rm b} = \sum_{j=1}^{N}\left[p_j^2/(2m_j) + m_j\omega_j^2 x_j^2/2\right]$. The coupling between them is assumed in form $H_{\rm sb} = f(x)\sum_{j=1}^{N} c_j x_j$ with some real function $f(\cdot)$.

The projection scheme of Nakajima and Zwanzig (*9*) allows us to separate the dynamics of system and bath. The thermal state of the bath is represented by the canonical density operator $\rho_{\rm b}^{\rm eq} = \exp(-\beta H_{\rm b})/Z_{\rm b}$ with a given temperature $T = (k_B\beta)^{-1}$ and $Z_{\rm b}$ being the partition function of the bath. Applying a projector $P = \rho_{\rm b}^{\rm eq}{\rm tr}_{\rm b}$ with ${\rm tr}_{\rm b}\rho_{\rm b}^{\rm eq} = 1$ and $Q = (1-P)$ yields an exact formal quantum master equation for the time evolution of the reduced system density operator $\rho_{\rm s}$ (*7*) in the form

$$\begin{aligned}
\dot{\rho}_{\rm s}(t) &= \mathcal{L}_{\rm s}^{\rm eff}\rho_{\rm s}(t) + \int_0^t dt' K(t,t')\rho_{\rm s}(t') + \Gamma(t),\\
\mathcal{L}_{\rm s}^{\rm eff} &= \mathcal{L}_{\rm s} + \lambda\,{\rm tr}_{\rm b}\mathcal{L}_{\rm sb}\rho_{\rm b}^{\rm eq} + \lambda^2\mathcal{L}_{\rm ren},\\
K(t,t') &= \lambda\,{\rm tr}_{\rm b}\mathcal{L}_{\rm sb}\left(\mathcal{T}e^{\int_{t'}^{t} Q\mathcal{L}dt''}\right)Q(\mathcal{L}_{\rm b} + \lambda\mathcal{L}_{\rm sb})\rho_{\rm b}^{\rm eq},\\
\Gamma(t) &= \lambda\,{\rm tr}_{\rm b}\mathcal{L}_{\rm sb}\left(\mathcal{T}e^{\int_{0}^{t} Q\mathcal{L}dt''}\right)Q\rho_{\rm tot}(0).
\end{aligned} \tag{S3}$$

Here, $\rho_{\rm tot}(0)$ is the total density operator of system and bath at initial time. The Liouville superoperators $\mathcal{L}_{\rm s}$, $\mathcal{L}_{\rm sb}$ and $\mathcal{L}_{\rm ren}$ are associated with corresponding Hamiltonian operators. Moreover,

$\mathcal{L}_{\rm s}^{\rm eff} = -i[H_{\rm s}+H_{\rm ren},\cdot]$ and $\mathcal{T}$ is the time-ordering operator (*10*). Next, we expand the correlated thermal equilibrium state to the first order in the overall coupling strength λ and obtain

$$\rho^{\rm eq} \approx \frac{1}{Z_{\rm s}}\frac{1}{Z_{\rm b}}e^{-\beta(H_{\rm s}+H_{\rm b})} - \lambda\frac{1}{Z_{\rm s}}\frac{1}{Z_{\rm b}}\int_0^\beta d\beta' e^{-(\beta-\beta')(H_{\rm s}+H_{\rm b})}H_{\rm sb}^{(1)}e^{-\beta'(H_{\rm s}+H_{\rm b})}, \tag{S4}$$

with the respective partition functions $Z_{\rm tot} = {\rm tr}\exp(-\beta H_{\rm tot})$, $Z_{\rm b} = {\rm tr}_{\rm b}\exp(-\beta H_{\rm b})$ and $Z_{\rm s} = {\rm tr}_{\rm s}\exp(-\beta H_{\rm s})$. Next, we take the trace over the system degrees of freedom on both sides of Eq. (S4) and get

$$\rho_{\rm b}^{\rm eq} = \frac{1}{Z_{\rm b}}e^{-\beta H_{\rm b}} + \frac{\lambda\chi}{Z_{\rm b}}\int_0^\beta d\beta' e^{-(\beta-\beta')H_{\rm b}}\left(\sum_{i=1}^N c_i x_i\right)e^{-\beta' H_{\rm b}}. \tag{S5}$$

Here, $\chi = (1/Z_{\rm s}){\rm tr}_{\rm s}\left[f(x)e^{-\beta H_{\rm s}}\right]$. The well-known bath correlation function

$$c(t) = \int_{-\infty}^{\infty}\frac{d\omega}{2\pi}J(\omega)\cos(\omega t)\coth\left(\frac{\beta\omega}{2}\right) - i\int_{-\infty}^{\infty}\frac{d\omega}{2\pi}J(\omega)\sin(\omega t) \equiv a(t) - ib(t) \tag{S6}$$

is given in terms of the standard bath spectral density $J(\omega)$ and has the real part $a(t)$ and imaginary part $b(t)$. After inserting Eqs. (S4) and (S5) into Eq. (S3), we can express the last three terms of Eq. (S3) by $a(t)$ and $b(t)$ and obtain

$$\begin{aligned}
\mathcal{L}_{\rm s}^{\rm eff} &= \mathcal{L}_{\rm s} + \lambda^2\mu\mathcal{L}_{\rm ren,s} + \lambda^2\chi\mu\mathcal{L}^-, \\
K(t,t') &= \lambda^2\mathcal{L}^-\left(a(t-t')\mathcal{T}e^{\int_{t'}^t\mathcal{L}_{\rm s}dt''}\mathcal{L}^- + b(t-t')\mathcal{T}e^{\int_{t'}^t\mathcal{L}_{\rm s}dt''}\mathcal{L}^+\right), \\
\Gamma(t) &= \lambda^2\mathcal{L}^-\int_{-\infty}^0 dt'\left[a(t-t')\mathcal{T}e^{\int_{t'}^t\mathcal{L}_{\rm s}dt''}\mathcal{L}^-\rho_{\rm s}^{\rm eq} + b(t-t')\mathcal{T}e^{\int_{t'}^t\mathcal{L}_{\rm s}dt''}\mathcal{L}^+\rho_{\rm s}^{\rm eq}\right],
\end{aligned} \tag{S7}$$

with $\mathcal{L}^- = -i[H_{\rm sb},\cdot]$ and $\mathcal{L}^+ = [H_{\rm sb},\cdot]_+ - 2\chi$. In terms of the spectral density, the potential renormalization is given by $\mu = \int_{-\infty}^{\infty}\frac{d\omega}{2\pi}J(\omega)/\omega$.

In order to obtain an analytic form of the bath correlation function, any given spectral density (in our particular case, we use the standard Ohmic form) can be approximated by a sum of Lorentzian-like spectral terms (*11, 12*) in the form

$$J(\omega) = \frac{\pi}{2}\sum_{k=1}^n\frac{p_k\omega}{[(\omega+\Omega_k)^2+\Gamma_k^2][(\omega-\Omega_k)^2+\Gamma_k^2]}, \tag{S8}$$

where the spectral amplitude p_k, the frequency Ω_k and the width Γ_k follows from the expansion of the original function in terms of Lorentzian functions. Inserting the expanded form of $J(\omega)$

in Eq. (S6) results in

$$
\begin{aligned}
a(t) &= \sum_{k=1}^{n} \frac{p_k}{8\Omega_k\Gamma_k} \coth\left[\frac{\beta}{2}\left(\Omega_k + i\Gamma_k\right) e^{i\Omega_k t - \Gamma_k t}\right] + \sum_{k=1}^{n} \frac{p_k}{8\Omega_k\Gamma_k} \coth\left[\frac{\beta}{2}\left(\Omega_k - i\Gamma_k\right) e^{-i\Omega_k t - \Gamma_k t}\right] \\
&\quad + \frac{2i}{\beta} \sum_{k=1}^{n'} J(i\nu_k) e^{-\nu_k t}, \\
b(t) &= \sum_{k=1}^{n} \frac{ip_k}{8\Omega_k\Gamma_k} \left(e^{i\Omega_k t - \Gamma_k t} - e^{-i\Omega_k t - \Gamma_k t}\right),
\end{aligned}
\tag{S9}
$$

with the Matsubara frequencies $\nu_k = 2\pi k/\beta$.

Next, we rewrite the correlation functions as $a(t) = \sum_{k=1}^{n_r} \alpha_k^r e^{\gamma_k^r t}$ and $b(t) = \sum_{k=1}^{n_i} \alpha_k^i e^{\gamma_k^i t}$ with $n_i = 2n$, $n_r = 2n + n'$, where n' is the number of Matsubara frequencies used. Then we define new auxiliary "density matrices" which incorporate both memory effects and initial correlations according to

$$
\begin{aligned}
\rho_k^r(t) &= \lambda \left(\mathcal{T} e^{\int_0^t dt' \mathcal{L}_\mathrm{s}} e^{\gamma_k^r t} \int_0^\infty dt' e^{\mathcal{L}_\mathrm{s} t'} e^{\gamma_k^r t'} \mathcal{L}^- \rho_\mathrm{s}^\mathrm{eq} + \int_0^t dt' e^{\gamma_k^r (t-t')} \mathcal{T} e^{\int_{t'}^t dt'' L_\mathrm{s}} \mathcal{L}^- \rho_\mathrm{s}(t') \right), \\
\rho_k^i(t) &= \lambda \left(\mathcal{T} e^{\int_0^t dt' \mathcal{L}_\mathrm{s}} e^{\gamma_k^i t} \int_0^\infty dt' e^{\mathcal{L}_s t'} e^{\gamma_k^i t'} \mathcal{L}^+ \rho_s^\mathrm{eq} + \int_0^t dt' e^{\gamma_k^i (t-t')} \mathcal{T} e^{\int_{t'}^t dt'' L_\mathrm{s}} \mathcal{L}^+ \rho_\mathrm{s}(t') \right).
\end{aligned}
\tag{S10}
$$

The time-retarded Eq. (S3) (first term) can the be deconvoluted into a set of coupled first-order equations in the form

$$
\begin{aligned}
\dot{\rho}_\mathrm{s}(t) &= \mathcal{L}_\mathrm{s}^\mathrm{eff}(t)\rho_\mathrm{s}(t) + \lambda \left[\sum_{k=1}^{n_r} \alpha_k^r \mathcal{L}^- \rho_k^r(t) + \sum_{k=1}^{n_i} \alpha_k^i \mathcal{L}^- \rho_k^i(t) \right], \\
\dot{\rho}_k^r(t) &= [\mathcal{L}_\mathrm{s}(t) + \gamma_k^r]\rho_k^r(t) + \lambda \mathcal{L}^- \rho_\mathrm{s}(t), k = 1, \ldots, n_r, \\
\dot{\rho}_k^i(t) &= [\mathcal{L}_\mathrm{s}(t) + \gamma_k^i]\rho_k^i(t) + \lambda \mathcal{L}^+ \rho_\mathrm{s}(t), k = 1, \ldots, n_i.
\end{aligned}
\tag{S11}
$$

This set of time non-local quantum master equations was used for the calculations of the quantum system dynamics.

Calculation of the absorption and the circular dichroism (CD) spectrum

We have used the first-order transition dipole moment correlation function to calculate the absorption and the circular dichroism spectra using the expressions

$$
\begin{aligned}
I(\omega) &\propto \omega \int_{-\infty}^{+\infty} dt e^{i\omega t} \langle \boldsymbol{\mu}(t) \boldsymbol{\mu}(0) \rangle_g, \\
CD(\omega) &\propto \omega \int_{-\infty}^{+\infty} dt e^{i\omega t} \langle \boldsymbol{R}_{m,n} \cdot \boldsymbol{\mu}_m \times \boldsymbol{\mu}_n(t) \rangle_g.
\end{aligned}
\tag{S12}
$$

Here, $\boldsymbol{\mu}$ is the transition dipole moment, the subscript g means performing the trace in the correlation function over a thermally equilibrated bath, and, $\boldsymbol{R}_{m,n}$ is the position vector between monomers m and n. The correlation function can be calculated as $\langle \boldsymbol{\mu}(t)\boldsymbol{\mu}(0)\rangle_g = \mathrm{tr_s}\{\boldsymbol{\mu}\mathrm{tr_b}[e^{-iHt}\boldsymbol{\mu}\rho_g e^{iHt}]\}$, $\langle \boldsymbol{R}_{m,n}\cdot\boldsymbol{\mu}_m \times \boldsymbol{\mu}_n(t)\rangle_g = \mathrm{tr_s}\{\boldsymbol{R}_{m,n}\cdot\boldsymbol{\mu}_m \times \mathrm{tr_b}[e^{-iHt}\boldsymbol{\mu}_n\rho_g e^{iHt}]\}$.

Calculation of 2D electronic spectra

For the calculation of the 2D spectra we have applied the equation of motion-phase matching approach (EOM-PMA) proposed by Gelin et al. (*13*). In the EOM-PMA, the induced polarization in the photon-echo direction is calculated by simultaneous propagation of three auxiliary density matrices (ρ_1, ρ_2, ρ_3), each of which obeys a modified equation of motion of the form

$$\begin{aligned}
\dot{\rho_1}(t) &= -i[H_s - V_1(t,t_1) - V_2^\dagger(t,t_2) - V_3^\dagger(t,t_3), \rho_1(t)] - \Re(t)\rho_1(t),\\
\dot{\rho_2}(t) &= -i[H_s - V_1(t,t_1) - V_2^\dagger(t,t_2), \rho_2(t)] - \Re(t)\rho_2(t),\\
\dot{\rho_3}(t) &= -i[H_s - V_1(t,t_1) - V_3^\dagger(t,t_3), \rho_3(t)] - \Re(t)\rho_3(t),
\end{aligned} \tag{S13}$$

where $V_\alpha(t,t_\alpha) = XAe^{-(t-t_\alpha)^2/2\Gamma^2}e^{i\omega t}$, X, Γ are the transition dipole operator and pulse duration, respectively, and $\Re$ is a relaxation superoperator. All three above master equations were calculated by the time non-local quantum master equation Eq. (S11) with the respective different time-dependent Hamiltonians. Then, the third-order induced polarization can be synthesized as

$$P_{PE}(t_1,t_2,t_3,t) = e^{i\mathbf{k_s}\cdot\mathbf{r}}\langle X(\rho_1(t) - \rho_2(t) - \rho_3(t))\rangle + c.c., \tag{S14}$$

where the brackets $\langle \ldots \rangle$ indicate the evaluation of the trace.

The total 2D Fourier-transformed spectrum is then given by the double Fourier transform of the photon-echo polarization signal with respect to τ (which is the time delay between t_1 and t_2) and t, i.e.,

$$S_{PE}(\omega_\tau, T, \omega_t) \sim \int d\tau \int dt\, e^{-i\omega_\tau\tau}e^{i\omega_t t}P_{PE}(\tau,T,t), \tag{S15}$$

where ω_τ is the "coherence" frequency, ω_t is the detection frequency, and T is "waiting" time (delay between t_2 and t_3).

For the calculation of the 2D spectra of the FMO complex, a multi-processing interface has been used to reduce simulation time. The coherent time period $[-300, 300]$ fs has been split up into steps of size $d\tau = 10$ fs and each specified time was sent to one CPU for the calculation. 500 realizations were calculated to account for the random rotation of the molecular transition dipole moment and for static disorder. Therefore, 61 CPUs were used for the calculation of one spectrum. For each CPU, the maximally available memory space of 3.5 GByte was used to speed up the calculation.

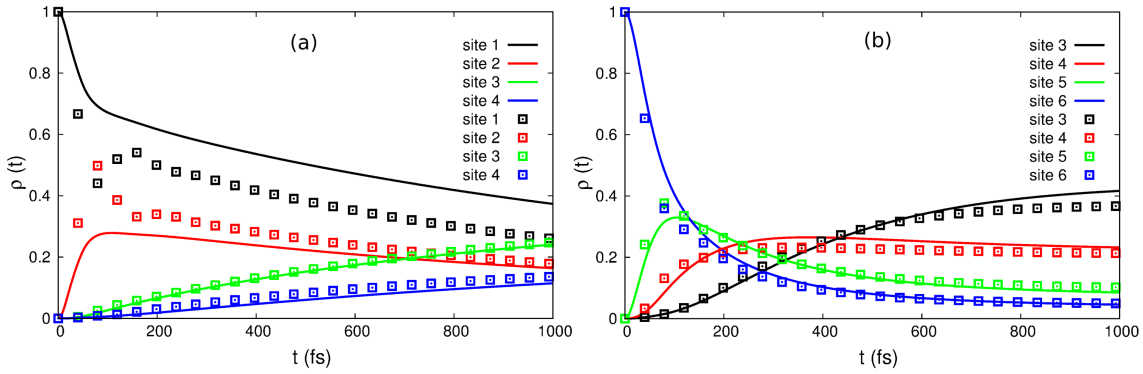

Figure S4: Time-dependent populations of the FMO sites $1-4$ (a) and $3-6$ (b) obtained for the initial preparation in site 1 (a) or in site 6 (b). The solid lines mark the results obtained from a time-nonlocal quantum master equation used in this work together with the spectral density Eq. (S1). The symbols show the results of an exact path-integral calculations (*15*) on the basis of an independently obtained and parametrized experimental spectral density (*14*).

Dynamics of the population of the FMO sites

The spectral density given in Eq. (S1) is the result of a simultaneous fitting to the experimental photon absorption and circular dichroism spectra. A further test of its reliability can be obtained by comparing the resulting dynamics of the FMO site populations obtained with the spectral density of Eq. (S1) and that one obtained previously from numerically exact path integral calculations with an independently obtained and parametrized experimental spectral density (*14*). To be specific, we use the numerically exact results of Ref. 15 as a reference and consider the two cases in which either site 1 or 6 is chosen as the initial state. The system Hamiltonian used in Ref. 15 is exactly the same as used here. The spectral density of Ref. 14 used in Ref. 15 is different from that of Eq. (S1). The low-frequency part of Eq. (S1) is Ohmic while that one of Ref. 14 is super-Ohmic. The high-frequency parts are also different, but we note that the interesting long-time dynamics is governed by the low-frequency parts of the bath spectral density. The comparison is shown in Fig. S4 for a temperature of 300 K. We find a good agreement especially at long times while the deviations at short times are due to the differences in the high-frequency sections of the two different spectral densities.

Low-temperature calculations

In order to check the performance of the modeling and the reliability of the approach in terms of a quantum dissipative dynamics, we consider in this section the impact of changing the temperature, but keeping all other parameters unchanged. For this, we have calculated the linear absorption and CD spectra at 77 K. The calculated results are shown in Fig. S5 (red solid lines) together with the experimentally measured data taken from Ref. 16. We find a good agreement

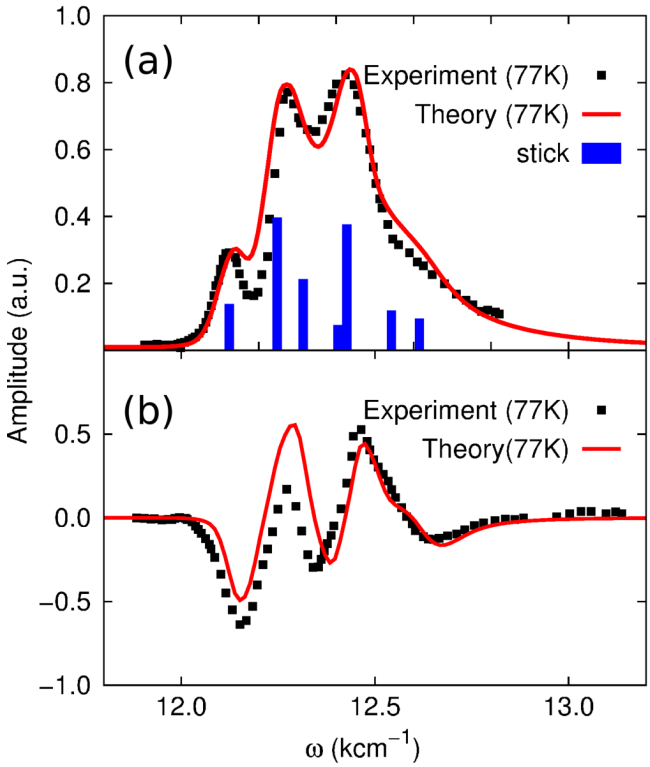

Figure S5: (a) Linear absorption spectrum and (b) circular dichroism spectrum of the FMO complex at 77 K. The solid red lines show the theoretical results obtained with the same parameter set used throughout this work, but with the only modified parameter being temperature. The square symbols mark the experimental results taken from Ref. 16. The blue bars in (a) mark the stick spectrum of the FMO complex.

given the fact that we the only changing parameter is temperature.

In addition, we have calculated the 2D electronic spectra of the FMO complex at 77 K as well with the same set of parameters. The results for different waiting times are shown in Fig. S6. The spectra are in good agreement with the experimental results (*17, 18*). The energy transfer dynamics and pathways can be clearly observed by the kinetics of the off-diagonal peaks.

Moreover, we calculate the time evolution of the off-diagonal signal at the spectral position ($\omega_\tau = 12350$ cm^{-1}, $\omega_t = 12200$ cm^{-1}) considered in Ref. 19 and marked by "X" in Fig. 1A in the main paper, but now also for 77 K. Apart from changing temperature, we use the same parameters as before and the spectral density of Eq. (S1). The results for the real and imaginary parts are shown in Fig. S7. We find only weak electronic coherence which vanishes within the dephasing time of less than 200 fs. As a consistence check, we also measure the homogeneous linewidth provided by the antidiagonal in Fig. S6 for zero waiting time. We find a FWHM of

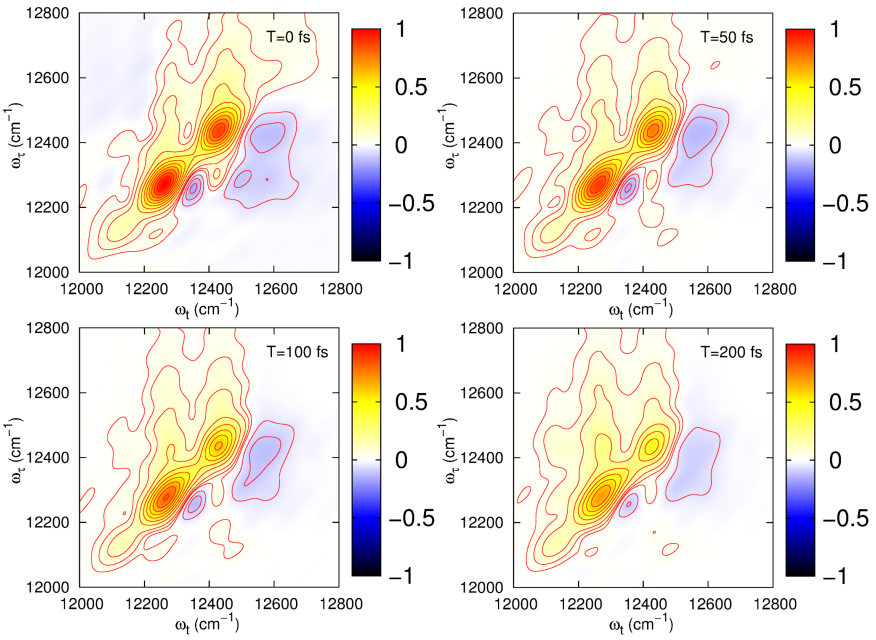

Figure S6: Real part of the 2D photon echo spectra calculated for a temperature of 77 K for selected waiting times as indicated. Notice that the two axes for ω_τ and ω_t are swapped as compared to Ref. (*17*).

$\Delta_{\mathrm{hom}} = 90\ \mathrm{cm}^{-1}$. This corresponds to an electronic dephasing time of $\tau_{\mathrm{hom}} = 120$ fs at 77 K, in agreement with the previous results. Hence, we cannot confirm long-lived electronic coherence at a temperature of 77K reported up to times beyond 1 ps.

Simulating long-lived electronic coherence

We did not observe long-lived electronic coherence in the present experimental and theoretical results of the FMO complex. However, we can consider the question how a long-lived electronic coherence would show up in an optical 2D spectrum at low temperature and, consistently, in the time-dependent off-diagonal signal. To answer this question, we have used the simplest possible model of a pure Ohmic spectral density, i.e., only the first term of Eq. (S1) and mimic long-lived electronic coherence by a very weak system-bath interaction. We set $\gamma = 0.35$ and $\omega_c = 100\ \mathrm{cm}^{-1}$, and set the temperature again to 77 K. In Fig. S8 (a), we show the result of the 2D spectrum of the FMO under these weak-coupling conditions. The weak system-bath coupling induces a very narrow central peak with a small homogeneous broadening visible in the antidiagonal band width. We extract a FWHM of $\Delta_{\mathrm{hom}} = 25\ \mathrm{cm}^{-1}$. This corresponds to an electronic dephasing time of $\tau_{\mathrm{hom}} = 420$ fs.

Correspondingly, we show in Fig. S8 (b) the time-dependent off-diagonal signal at the spec-

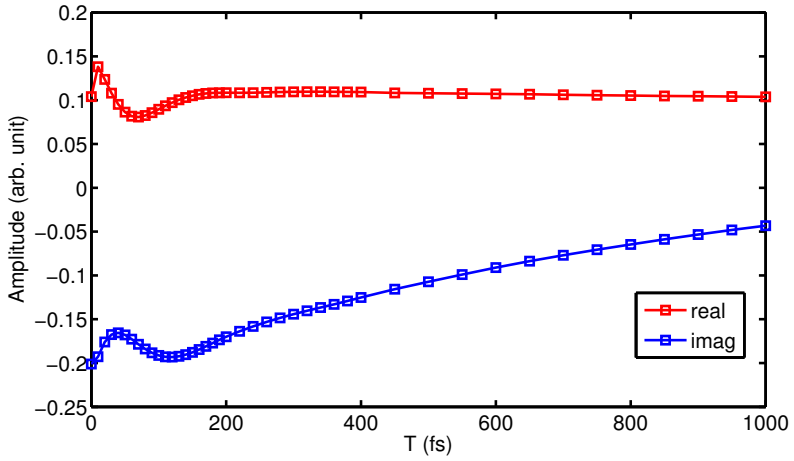

Figure S7: Calculated time-dependent off-diagonal signal (red: real part, blue: imaginary part) at the spectral position ($\omega_\tau = 12350$ cm^{-1}, $\omega_t = 12200$ cm^{-1}) considered in Ref. 19 and marked by "X" in Fig. 1A in the main paper, but now for 77 K.

tral position ($\omega_\tau = 12350$ cm^{-1}, $\omega_t = 12200$ cm^{-1}) considered in Ref. 19 and marked by "X" in Fig. 1A in the main paper. We find (artificially created) long-lived electronic coherence up to times beyond 450 fs, in agreement with the findings from the homogeneous line width. However, the measured 2D spectra of the real FMO complex do not show these sharp ridges with a very narrow diagonal peaks at zero waiting times.

Three-dimensional spectrum of residuals in 2D data

After obtaining the residuals by removing the kinetics from the experimental data, we have applied a numerical Fourier transform to the real part with equally separated time steps (10 fs) up to 2 ps. This yields a three-dimensional spectrum of the residuals with the dimensions ω_t, ω_τ and the vibrational frequency in the waiting time domain, ω_T. A few representative two-dimensional vibrational maps with relatively large magnitudes and obtained from the experimental data are shown for different vibrational frequencies ω_T in Figs. S9 and S10. In order to prove the reproducibility of the observed vibrational oscillations, we present four data sets labeled by (1), (2), (3) and (4) of repeated measurements. In sets (1) and (2), the data were taken with a low power excitation pulse (with ~ 8 nJ), while in sets (3) and (4), we have chosen excitation pulse with ~ 12 nJ. It shows that the presented vibrational oscillations and the underlying frequencies are fully reproducible in four independent measurements although the excitation power was different.

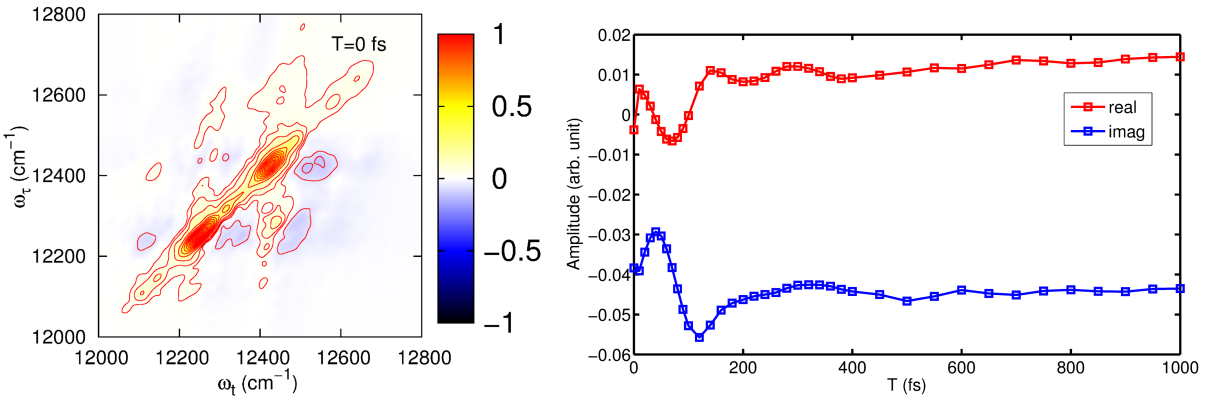

Figure S8: (a) Calculated 2D spectrum of the FMO under artificially assumed weak system-bath conditions with an Ohmic spectral density with $\gamma = 0.35$ and $\omega_c = 100$ cm^{-1}, and temperature of 77 K. Notice that the two axes for ω_τ and ω_t are swapped as compared to Ref. (*17*). (b) Extracted time-dependent off-diagonal signal at the spectral position ($\omega_\tau = 12350$ cm^{-1}, $\omega_t = 12200$ cm^{-1}) considered in Ref. 19 and marked by "X" in Fig. 1A in the main paper.

Correlation analysis of the 2D vibrational maps

In order to quantify the correlation in the presented 2D vibrational maps, we perform a 2D correlation analysis of the different sets of measurements which are labeled as (1) to (4) in Fig. S9 and S10. The correlation parameters are shown in Table 1.

Items	596	628	725	741	838	1015	1112	1144	1289	1595
1↔2	0.9218	0.8892	0.8571	0.7863	0.7531	0.7808	0.5801	0.8878	0.9202	0.7287
1↔3	0.6289	0.7929	0.7568	0.8485	0.6650	0.8688	0.5220	0.7912	0.7773	0.7065
1↔4	0.6591	0.7278	0.5807	0.6281	0.6190	0.8742	0.5826	0.7748	0.4268	0.6262
2↔3	0.7945	0.6009	0.7844	0.9047	0.4902	0.6668	0.8353	0.7655	0.8232	0.8208
2↔4	0.7600	0.5453	0.5885	0.6458	0.5040	0.6523	0.7551	0.7516	0.4439	0.7965
3↔4	0.8686	0.9498	0.7682	0.7624	0.9178	0.9514	0.4668	0.9739	0.6836	0.9409

Table 1: The 2D correlation analysis of the 2D vibrational maps. The vibrational frequencies are given in units of cm^{-1}.

Time-dependent off-diagonal signal at the X position

In Fig. 3C of the main paper, we show the time-dependent off-diagonal signal at the spectral position ($\omega_\tau = 12350$, $\omega_t = 12200$cm-1) considered in Ref. 19 and marked by "X" in Fig. 1A in the main paper for waiting times up to 600 fs. In Fig. S11, we provide the results for the time window between 600 fs and 2 ps in order to illustrate that no long-time electronic coherence is present up to this time. The data are the averages of four independently measured spectra with

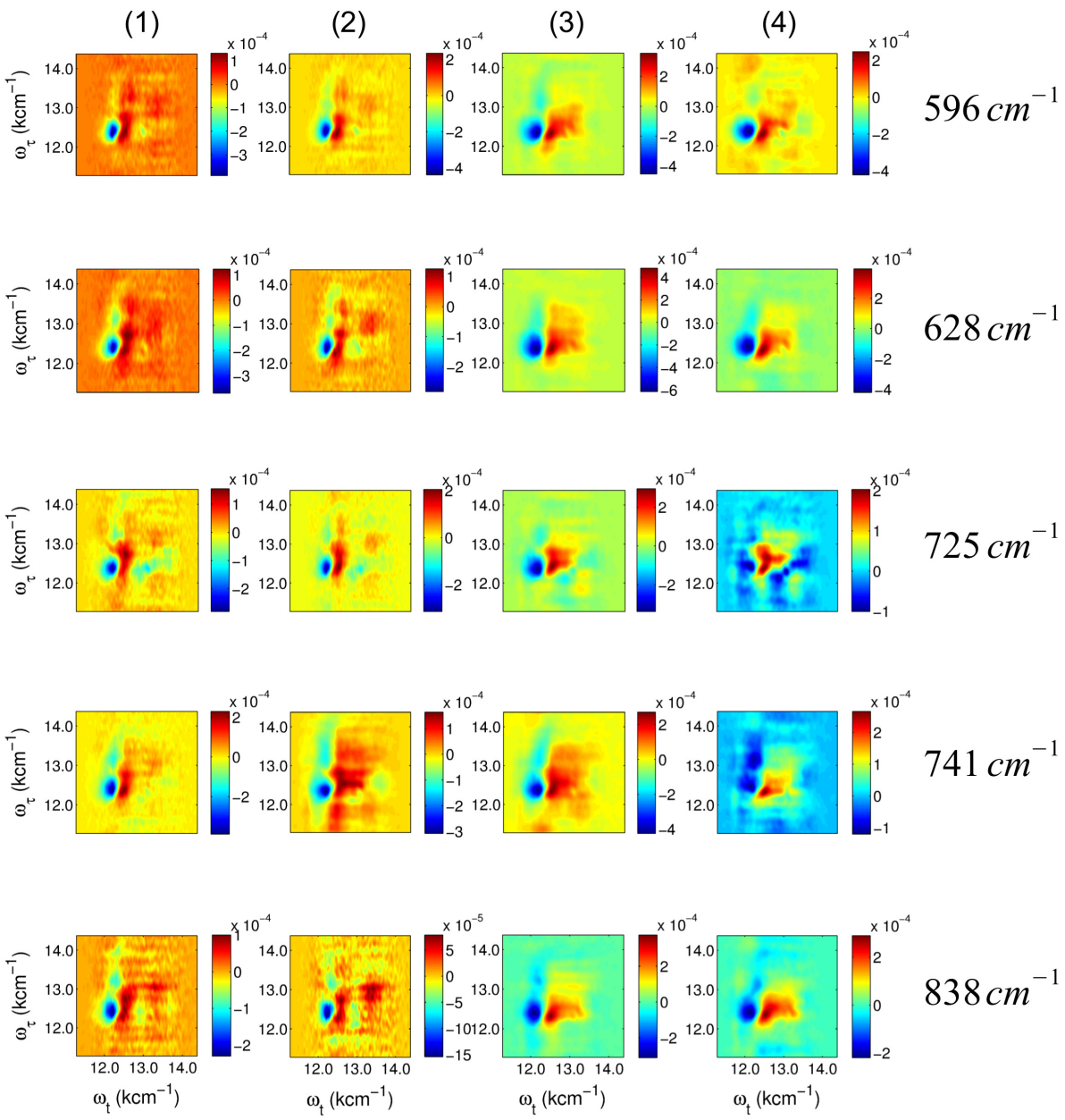

Figure S9: Two-dimensional vibrational map (ω_t, ω_τ) for different values of the frequency ω_T from 596 cm^{-1} to 838 cm^{-1}. Shown are four independent measurements with different values of the pulse excitation power. In sets (1) and (2), we have chosen $\sim$ 8 nJ and in sets (3) and (4), the excitation power was set to $\sim$ 12 nJ. All show good agreement and reproducibility.

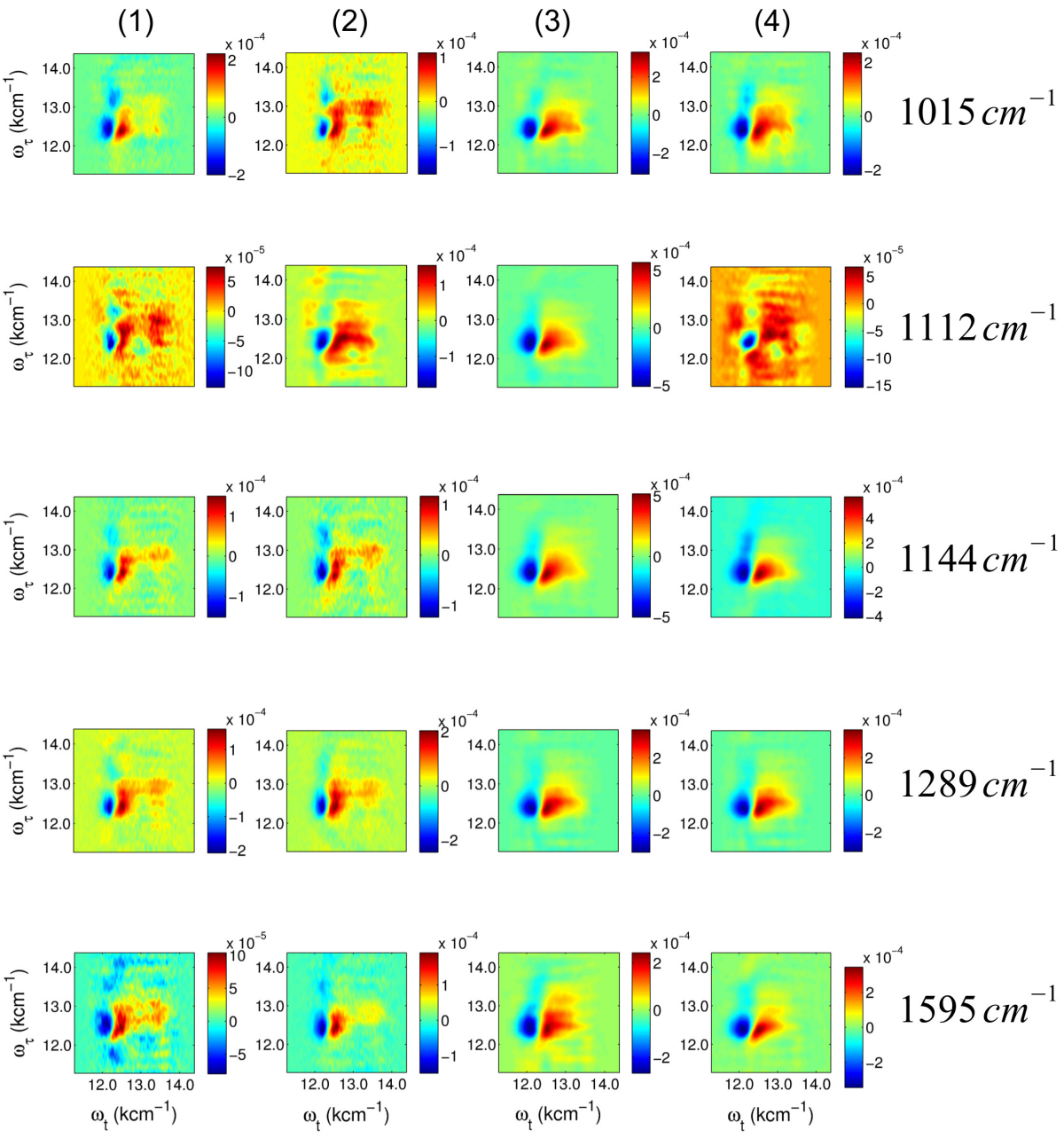

Figure S10: Same as in Fig. S9, but for the frequencies ω_T from 1015 cm^{-1} to 1595 cm^{-1}.

the resulting standard deviation shown as error bars.

Finally, we have calculated the Fourier spectrum of this average, which is shown in Fig.

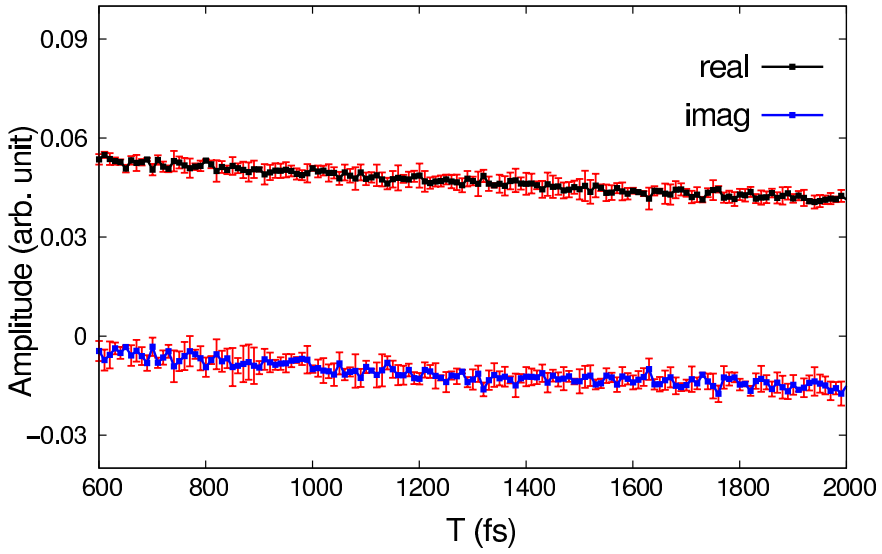

Figure S11: Time-dependent off-diagonal signal at the spectral position ($\omega_\tau = 12350$, $\omega_t = 12200$cm-1) considered in Ref. 19 and marked by "X" in Fig. 1A in the main paper for waiting times between 600 fs and 2 ps. The error bars mark the standard deviation obtained after averaging four available experimental spectra.

S12. We do not find any pronounced frequency component.

Relation between the anti-diagonal bandwidth and the homogeneous line width

In order to demonstrate that the exciton dynamics in the FMO complex operates in the fast modulation limit, we have investigated the time dependence of the frequency correlation function $M(T)$ (*20, 21*). For a given waiting time T, it can be extracted from the 2D electronic spectra in the form of the ellipse eccentricity of the central peak according to the ratio

$$M(T) = \frac{(a^2 - b^2)}{(a^2 + b^2)}\,, \tag{S16}$$

where a is the major and b the minor axis of the ellipse, see Fig. S13. When this function decays exponentially with increasing T, the dynamics occurs in the fast modulation (or homogeneous) limit. Put differently, the time scales of the homogeneous and inhomogeneous broadening are well separated and an effective Markovian dynamics occurs. Then, the antidiagonal band width coincides with the electronic dephasing time (*20, 21*). Here, we have measured the time-evolved diagonal (a) and anti-diagonal (b) bandwidth from the 2D spectra for different waiting times T. The frequency correlation function $M(T)$ is plotted in Fig. S13 and shows a clear exponential decay at short to intermediate times (< 500 fs). Due to the admixture from the vibrational progression and the energy transfer (excited state absorption), it deviates from a

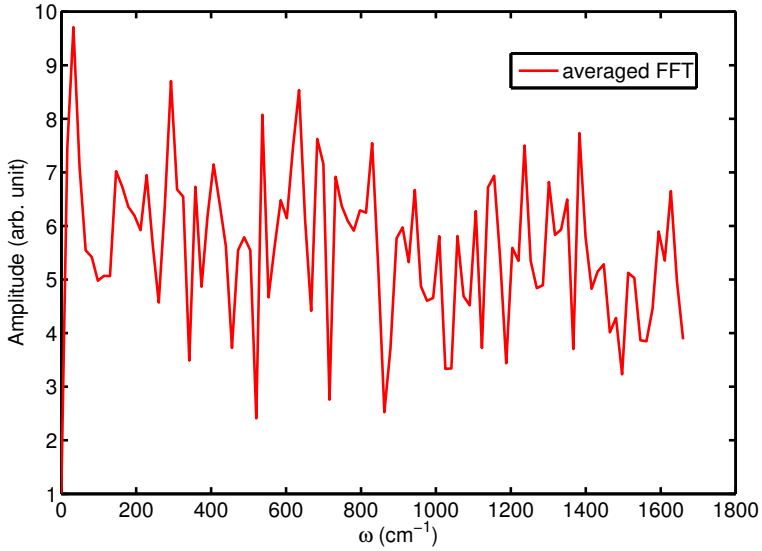

Figure S12: Fourier spectrum of the full time trace shown in Fig. 3C in the main paper and in Fig. S11.

clean single-exponential function at asymptotic times. Hence, we can safely conclude that we are in the Markovian (fast modulation) regime which confirms earlier findings (*22*) on the basis of numerically exact path-integral calculations of the non-Markovianity measure of the exciton dynamics of the FMO complex.

References

1. Azai C, Kim K, Kondo T, Harada J, Itoh S, Oh-Oka H (2011) A heterogeneous tag-attachment to the homodimeric type 1 photosynthetic reaction center core protein in the green sulfur bacterium Chlorobaculum tepidum. *Biochim Biophys Acta* 1807:803-812.

2. Wahlund TM, Woese CR, Castenholz RW, Madigan MT (1991) A thermophilic green sulfur bacterium from New Zealand hot springs, Chlorobium tepidum sp. nov. *Arch Microbiol* 156:81-90.

3. Oh-Oka H, Kamei S, Matsubara H, Iwaki M, Itoh S (1995) Two molecules of cytochrome c function as the electron donors to P840 in the reaction center complex isolated from a green sulfur bacterium, Chlorobium tepidum. *FEBS Lett* 365: 30-34.

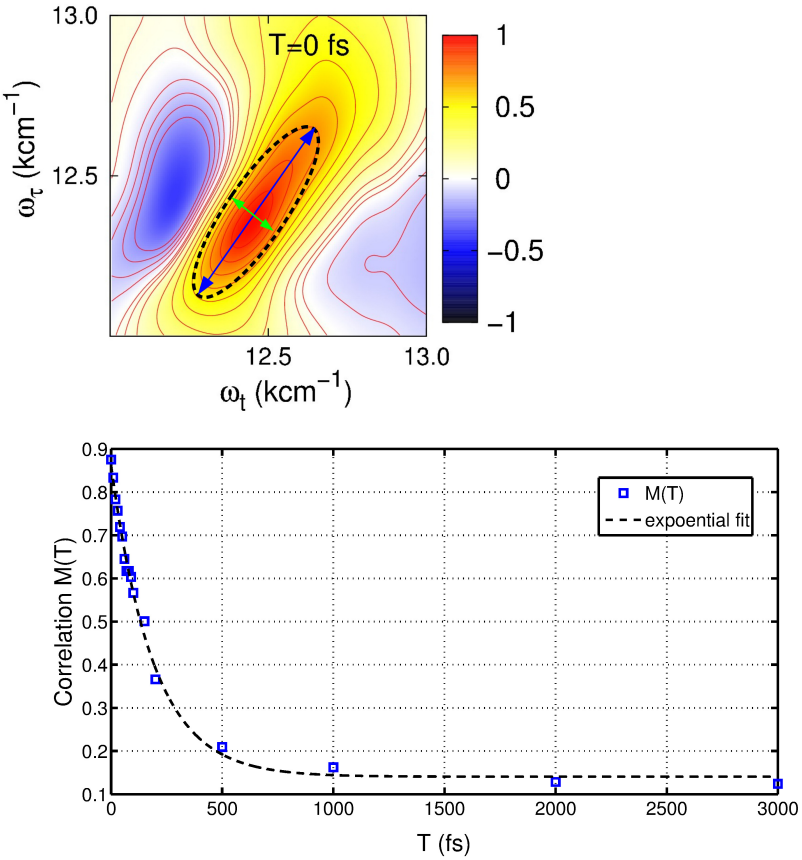

Figure S13: Time-evolution of the correlation function $M(T)$ calculated from the diagonal and anti-diagonal bandwidth. The dynamics can be well fitted by one exponential function, which clearly manifests the Markovian dynamics.

4. Kelly SM, Jess TJ, Price NC (2005) How to study proteins by circular dichroism. *Biochim Biophys Acta* 1751:119-139.

5. Greenfield NJ (2007) Using circular dichroism spectra to estimate protein secondary structure. *Nat Protoc* 1:2876-2890.

6. Gelzinis A, Valkunas L, Fuller FD, Ogilvie JP, Mukamel S, Abramavicius D (2013) Tight-binding model of the photosystem II reaction center: application to two-dimensional electronic spectroscopy. *New J Phys* 15:075013.

7. Meier C, Tannor DJ (1999) Non-Markovian evolution of the density operator in the pres-

ence of strong laser fields. *J Chem Phys* 111: 3365-3376.

8. Kleinekathöfer U (2004) Non-Markovian theories based on a decomposition of the spectral density. *J Chem Phys* 121:2505-2514.

9. Zwanzig R (1961) Statistical mechanics of irreversibility. *Lectures in Theoretical Physics (Boulder) Vol 3*, eds Britten WE, Downs BW, Downs J (Interscience, New York), pp 106 - 141.

10. Morillo M, Cukier RI (1997) Controlling low-temperature tunneling dynamics with external fields. *Phys Rev B* 54:13962-13973.

11. Kleinekathöfer U, Barvík I, Heřman P, Kondov I, Schreiber M (2003) Memory effects in the fluorescence depolarization dynamics studied within the B850 ring of purple bacteria. *J Phys Chem B* 107:14094-14102.

12. Ritschel G, Eisfeld A (2014) Analytic representations of bath correlation functions for ohmic and superohmic spectral densities using simple poles. *J Chem Phys* 141:094101.

13. Gelin MF, Egorova D, Domcke W (2005) Efficient method for the calculation of time- and frequency-resolved four-wave mixing signals and its application to photon-echo spectroscopy. *J Chem Phys* 123:164112.

14. Adolphs J, Renger T (2006) How Proteins Trigger Excitation Energy Transfer in the FMO Complex of Green Sulfur Bacteria. *Biophys J* 91:2778-2797.

15. Nalbach P, Braun D, Thorwart M (2011) Exciton transfer dynamics and quantumness of energy transfer in the Fenna-Matthews-Olson complex. *Phys Rev E* 84:041926.

16. Melkozernov AN, Olson JM, Li YF, Allen JP, Blankenship RE (1998) Orientation and excitonic interactions in the Fenna-Matthews-Olson bacteriochlorophyll a protein in membranes of the green sulfur bacterium Chlorobium tepidum. *Photosynth Res* 56: 315-328.

17. Thyrhaug E, Židek K, Dostál J, Bina D, Zigmantas D (2016) Exciton structure and energy transfer in the Fenna-Matthews-Olson complex. *J Phys Chem Lett* 7:1653-1660.

18. Brixner T, Stenger J, Vaswani HM, Cho M, Blankenship RE, Fleming GR (2005) Two-dimensional spectroscopy of electronic couplings in photosynthesis. *Nature* 434:625-628.

19. Panitchayangkoon G et al. (2010) Long-lived quantum coherence in photosynthetic complexes at physiological temperature. *Proc Natl Acad Sci USA* 107:12766-12770.

20. Hamm P, Zanni M (2011) Homogeneous and inhomogeneous dynamics. *Concepts and Methods of 2D Infrared Spectroscopy* (Cambridge University Press, Cambridge), pp 152 - 164.

21. Lazonder K, Pshenichnikov MS, Wiersma DA (2007) Two-dimensional optical correlation spectroscopy applied to liquid/glass dynamics. *Ultrafast Phenomena XV, Proceedings of the 15th International Conference*, eds Corkum P, Jonas DM, Miller RJD, Weiner AM (Springer, Berlin), pp 356 - 358.

22. Mujica-Martinez C, Nalbach P, Thorwart M (2013) Quantification of non-Markovian effects in the Fenna-Matthews-Olson complex. *Phys Rev E* 88:062719.